Article:
Kuramitsu, Y., Mizuta, A., Sakawa, Y. et al. (2016) TIME EVOLUTION of KELVIN-HELMHOLTZ VORTICES ASSOCIATED with COLLISIONLESS SHOCKS in LASER-PRODUCED PLASMAS. Astrophysical journal. 93. ISSN: 1538-4357

https://doi.org/10.3847/0004-637X/828/2/93

The Astrophysical Journal, 828:93 (10pp), 2016 September 10 doi:10.3847/0004-637X/828/2/93

TIME EVOLUTION OF KELVIN–HELMHOLTZ VORTICES ASSOCIATED WITH COLLISIONLESS SHOCKS IN LASER-PRODUCED PLASMAS

Y. Kuramitsu[1], A. Mizuta[2], Y. Sakawa[3], H. Tanji[3], T. Ide[3], T. Sano[3], M. Koenig[4,5], A. Ravasio[4], A. Pelka[4,6], H. Takabe[6], C. D. Gregory[7], N. Woolsey[8], T. Moritaka[1], S. Matsukiyo[9], Y. Matsumoto[10], and N. Ohnishi[11]
[1] Department of Physics, National Central University, No. 300, Jhongda Rd., Jhongli, Taoyuan, 320, Taiwan; yasu@ncu.edu.tw
[2] Computational Astrophysics Laboratory, RIKEN, Wako 351-0198, Japan
[3] Institute of Laser Engineering, Osaka University, 2-6 Yamadaoka, Suita, Osaka, 565-0871, Japan
[4] Laboratoire pour l'Utilisation des Lasers Intenses, UMR 7605, CNRS—CEA—Université Paris VI—Ecole Polytechnique, F-91128 Palaiseau Cedex, France
[5] Institute for Academic Initiatives, Osaka University, Suita, Osaka 565-0871, Japan
[6] Helmholtz-Zentrum Dresden-Rossendorf, Bautzner Landstr. 400, D-01328 Dresden, Germany
[7] Rutherford Appleton Laboratory, Chilton, Didcot OX11 0QX, UK
[8] York Plasma Institute, Department of Physics, University of York, York, YO10 5DD, UK
[9] Department of Earth System Science and Technology, Kyushu University, 6-1 Kasuga-Koen, Kasuga, 816-8580, Fukuoka, Japan
[10] Graduate School of Science, Chiba University, 1-33 Yayoi-cho, Inage-ku, Chiba 263-8522, Japan
[11] Graduate School of Engineering, Thohoku University, 6-6-01 Aramakiazaaoba, Aoba-ku, Sendai, 980-8579 Japan
Received 2015 November 16; revised 2016 June 13; accepted 2016 June 29; published 2016 September 7

ABSTRACT

We report experimental results on Kelvin–Helmholtz (KH) instability and resultant vortices in laser-produced plasmas. By irradiating a double plane target with a laser beam, asymmetric counterstreaming plasmas are created. The interaction of the plasmas with different velocities and densities results in the formation of asymmetric shocks, where the shear flow exists along the contact surface and the KH instability is excited. We observe the spatial and temporal evolution of plasmas and shocks with time-resolved diagnostics over several shots. Our results clearly show the evolution of transverse fluctuations, wavelike structures, and circular features, which are interpreted as the KH instability and resultant vortices. The relevant numerical simulations demonstrate the time evolution of KH vortices and show qualitative agreement with experimental results. Shocks, and thus the contact surfaces, are ubiquitous in the universe; our experimental results show general consequences where two plasmas interact.

Key words: hydrodynamics – instabilities – plasmas – shock waves – turbulence – waves

1. INTRODUCTION

Kelvin–Helmholtz instability (KHI) is a universal phenomenon in various fluids and plasmas where velocity shears exist. Resultant vortices and turbulence are essential in many space and astrophysical phenomena, such as transportation of the solar wind to Earth's magnetosphere (Hasegawa et al. 2004), and they triggerstar formation in giant molecular clouds (Elmegreen 1998; Berné et al. 2010). In space plasmas, local variables are obtained by direct measurements with spacecraft, however, it is difficult to obtain their global structures. By contrast, in astrophysical phenomena, the global images are obtained from their emissions though local observations of physical quantities are inaccessible. Recent rapid growth of laser technologies allows us to model space and astrophysical phenomena in laboratories (Drake 1999; Remington et al. 1999, 2006; Takabe et al. 1999). For instance, collisionless shocks have been experimentally investigated in laser-produced counterstreaming plasmas (Morita et al. 2010, 2013; Kuramitsu et al. 2011, 2012; Kugland et al. 2012; Ross et al. 2012; Fox et al. 2013; Yuan et al. 2013; Huntington et al. 2015; Park et al. 2015). We first reported the relatively laminar density jump with optical interferometry in collisionless counterstreaming plasmas in the absence of an external magnetic field using the Shenguang II laser facility (Morita et al. 2010). In order to distinguish shock from contact surface we measured the emission jump and its time evolutions with self-emission optical pyrometry (SOP) with the Gekko XII (GXII) laser facility (Kuramitsu et al. 2011). The observed density and emission jumps in laser-produced plasmas are considered to be collisionless shocks, therefore, there must be an electric/magnetic field to decelerate or dissipate the upstream supersonic flows to downstream subsonic ones. In order to confirm this, we have performed proton radiography to measure the shock electric/magnetic field with the LULI2000 laser facility. We have reported the experimental results of a turbulent electric field driven by KHI associated with two collisionless shock waves (Kuramitsu et al. 2012). Due to the laser conditions of LULI2000, the counterstreaming plasmas are not symmetric; they can have different lateral expansions and thus transverse velocities. When two shock waves are excited in the counterstreaming plasmas, the shock surfaces are mainly perpendicular to the counterstreaming component, and the transverse components are not shocked. This causes the shear flows along the contact surface, which result in the KHI (Kuramitsu et al. 2012). With the OMEGA and OMEGA EP laser facilities, symmetric counterstreaming plasmas can be produced (Kugland et al. 2012; Ross et al. 2012). In the symmetric conditions, KHI is less effective, however, filamentation instability or Weibel instability can take place where the magnetic filaments grow in the shock transition region (Fox et al. 2013; Yuan et al. 2013; Huntington et al. 2015; Park et al. 2015). Currently verifications of collisionless shock formation due to Weibel-type instability are ongoing with the world largest laser facility, the National Ignition Facility.

Different laser configurations allow us to investigate different instabilities and relevant phenomena in the universe. Symmetric counterstreaming plasmas are considered to excite a pair of symmetric shock waves. In particle-in-cell simulations (PIC) the so-called injection method is often used to excite a shock wave. This corresponds to one of the pair of symmetric shock waves (Takabe et al. 2008). Asymmetric plasmas are

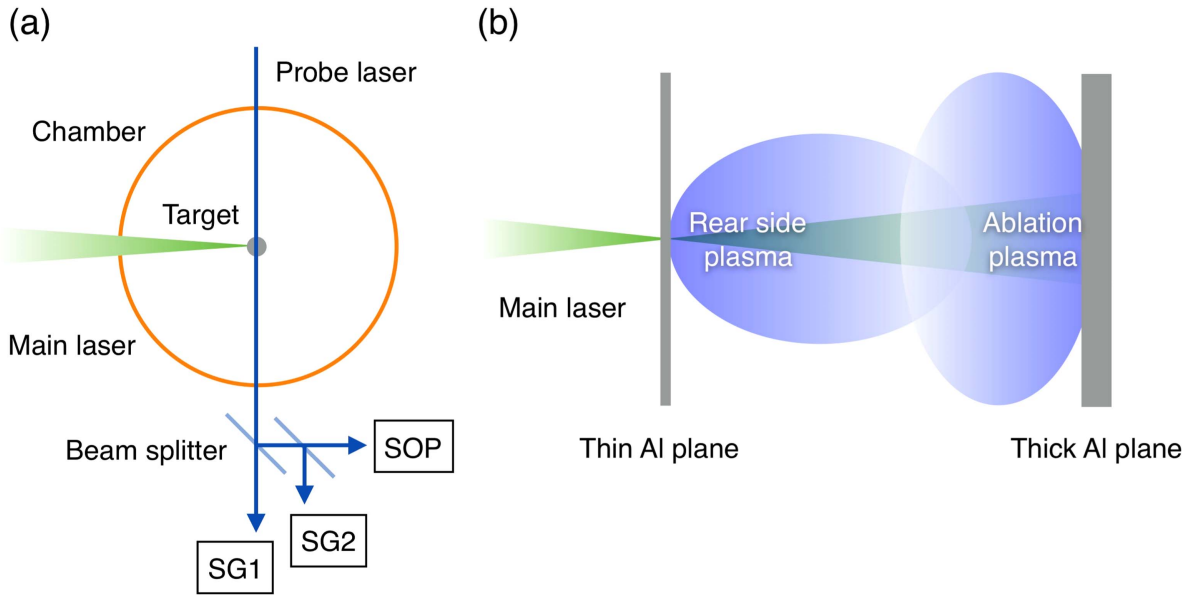

Figure 1. (a) The experimental setup is shown schematically including laser and diagnostics: SOP and SG stand for streaked optical pyrometry and shadowgraphy, respectively. (b) A schematic top view of the parallel double plane target is shown. The separation between two planes is 3 mm. The main laser irradiates both of the planes with a single shot, creating asymmetric counterstreaming plasmas.

more general; they can have different density, velocity, and temperature. Furthermore, asymmetric plasmas can have different divergence and structures, such as the solar wind plasma and the Earth's magnetospheric plasma (Hasegawa et al. 2004). In general, when two asymmetric plasmas interact, there can be shear flows between these plasmas. Where the shear flows exist, the KHI can grow, which can mix plasmas (Hasegawa et al. 2004), be a source of turbulence (Elmegreen 1998; Berné et al. 2010), and be a source of magnetic field (Alves et al. 2012). The KHI has also been an important subject in inertial confinement fusion. Shock tube experiments in high-energy-density plasmas with a rippled interface provide the KHI evolution in a controlled manner (see Hurricane et al. 2009, 2010, 2012; Harding et al. 2009). Counterpropagating shear experiments show KHI and its transition to turbulence in high-energy-density plasmas (Doss et al. 2013a, 2013b, 2015; Wang et al. 2015; Merritt et al. 2015).

In this paper we discuss the time evolution of KHI in laser-produced plasmas. In Section 2 we describe our experimental setup including laser, diagnostics, and target conditions. We follow the experiment in Kuramitsu et al. (2012) where we observed a turbulent electric field with proton radiography. Then, we show the results obtained from shadowgraphy and SOP. In Section 4 we perform numerical simulations in order to interpret the experimental results. We perform a radiative hydrodynamic (RHD) code to simulate the interaction between the laser and targets. Since the RHD simulations is costly and in order to resolve the hydrodynamic instability, we transfer the RHD results to high resolution hydrodynamic (HD) simulations. The HD simulations reproduce the time evolution of KHI. Finally Section 5 gives our discussion and summary.

2. EXPERIMENT

The experiment was performed with LULI2000 at the École Polytechnique in France. Figures 1(a) and (b) show the schematic configuration of the experiment and target, respectively. The target is ideally identical to that in Kuramitsu et al. (2012), however, the laser incident angle is different from that in the previous experiment. A double parallel plane target (distance of 3 mm) is irradiated with the main laser (energy of ~300 J on target at 527 nm wavelength, spot size of 400 μm with a phase plate, pulse duration of 1 ns) with a normal incidence with respect to the target surface. The laser beam is focused on the first plane (Al, thickness of 0.75 μm) with an $F = 4$ system and then burns through the first plane. The transmitted laser also irradiates the second plane (Al, thickness of 50 μm), forming fast counterstreaming plasmas. Two shock waves are expected to be excited, resulting from the interactions between plasmas. Since the laser is defocused at the second plane, the plasma from the second plane is slower and broader than that of the first plane. Therefore, the counterstreaming plasmas are asymmetric. A contact surface separates the two plasmas and due to the asymmetry there will be shear flows along the contact surface. The shear flows excite the KHI (Kuramitsu et al. 2012).

We briefly review the previous results (Kuramitsu et al. 2012), where we observed the transverse modulation along the contact surface with proton radiography. The laser incidence was 20° to the target normal, and thus the plasma from the second target observed with interferometry was flat and slow, implying ionization with X-rays from the laser–matter interaction from the first target. This results in a larger velocity and density difference between two plasmas from the first and second target than our current setting with the normal incidence of the laser. The growth rate of the KHI is written as $\gamma_{\rm KH} = k|v_1 - v_2|(\rho_1\rho_2)^{1/2}/(\rho_1 + \rho_2)$, where k and v are the wave number and plasma velocities along the contact, respectively, ρ is the mass density, and the subscripts 1 and 2 represent the plasmas from the first and second planes, respectively (Drake 2006). The wavelength of the observed transverse modulation is $0.5 \sim 1$ mm in the proton radiograph and also in the numerical simulation. The velocity difference has been estimated from the interferograms as the order of ~1000 km s^{-1} early time. The mass densities are estimated as follows. The pressure in the downstream regions

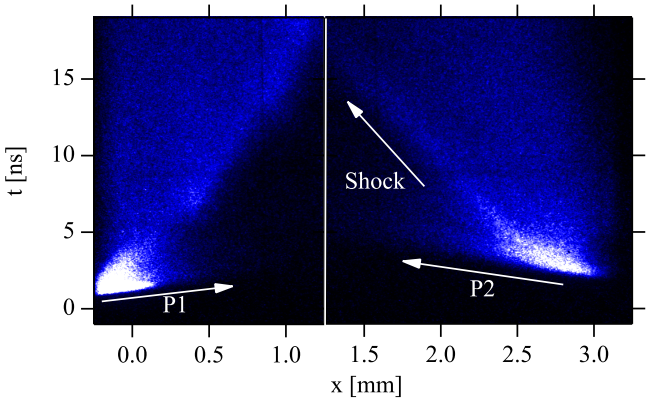

Figure 2. Combined image of streaked self-emission optical pyrometry (SOP). The laser comes from the left. Since the field of view is not enough to cover the double plane target, two images of SOP is combined to show the plasma evolutions from the both planes.

are balanced, $P_1 \sim P_2$, and the downstream pressure roughly equals to the upstream kinetic pressure; $n_1 m u_1^2/2 \sim P_1 \sim P_2 \sim n_2 m u_2^2/2$, where n is the number density in the upstream regions, m is the ion mass, and u is the upstream plasma velocity, which is normal to the contact. From the timing of the interferogram taken and the positions of the opaque regions, we can estimate the velocities of the plasma as 300 and 100 km s^{-1} from the first and second targets, respectively. Using these velocities as the upstream velocities, the number densities are estimated as $n_2 \sim 9\ n_1$, where $n_1 \sim 2 \times 10^{18}$ cm^{-3}. The downstream mass density is proportional to the upstream number density, and assuming strong shocks or equal proportionality for both plasmas, ρ_2 is also about an order higher than ρ_1. These estimations are consistent with numerical results. Using these values, we can estimate $\gamma_{\rm KH} \sim 2 \times 10^9$ s^{-1}. The KHI can evolve in our experimental timescale.

In this experiment we observe the time evolution of the plasmas and the instability with transverse diagnostics. In order to observe the plasma structures we use shadowgraphy with two independent intensified charged coupled devices (ICCDs, gate width of 120 ps), which are represented in Figure 1(a) as SG1 and SG2. The probe laser for the shadowgraphy is 3ω (355 nm) light to observe high-density contact regions. We also observe the emission from plasma at a wavelength of 420 nm using streak optical pyrometry, which is shown as SOP in Figure 1(a), providing plasma velocity.

3. RESULTS

Now we show our experimental results. Figure 2 shows the time evolution of the central regions of plasma emissions taken with SOP. The field of view of the SOP is less than the separation of the double plane target, thus, we combine two SOP images to cover the region of interest. The target positions ($x = 0$ and 3 mm) are determined from the reference images taken before the each shot. The nominal laser timing $t = 0$ ns is determined from timing shots. At the first plane $x = 0$ mm the emission starts to rise from $t \sim 0.7$ ns. There is a further delay at the second plane $x = 3$ mm; the emission starts to rise from $t \sim 1.7$ ns. We will discuss these delays with the simulation results later.

In the left panel of Figure 2 P1 indicates the rear side plasma from the first (left) target and the arrow corresponds to 850 km s^{-1}. In the right panel P2 indicates the plasma ablated with the transmitted laser from the second (right) plane. At the very beginning, the speed of the ablation plasma seems very fast, more than 1000 km s^{-1}. Slightly later, the emission edge seems slower, as indicated by the arrow P2 corresponding to 750 km s^{-1}. In the previous experiment, since we had just two snapshots of interferograms with a 2ω (532 ns) probe laser, we estimated the minimum relative velocity of the plasmas as 400–600 km s^{-1} (Kuramitsu et al. 2012). Since our results show a much higher relative velocity $\geqslant$1600 km s^{-1} than that of the previous experiment, the mean free paths of ions are much larger than the previous estimations. Therefore, the structures observed in our experimental system are considered to be from collisionless interactions of plasmas.

Although the two SOP images in Figure 2 are taken on different shots, we can see that a sharp structure, which is considered to be a collisionless shock (Kuramitsu et al. 2012) as indicated by the arrow labeled "Shock," appears when the P1 plasma reaches and starts to interact with the P2 plasma. Note that low-density and high-velocity plasmas can penetrate each other, and thus, a similar structure appears from the first plane when the P2 plasma reaches the rear side plasma. At $x \sim 0.5$ mm and $t \sim 7$ ns one can see the emission increase and the resultant sharp structure propagating toward the right. This is also considered to be a collisionless shock (Kuramitsu et al. 2013), and we also recognize this in the shadowgrams shown below. Here, however, we do not discuss this part; we focus on the shock structure near the second (right) target indicated with "Shock."

Figure 3 shows images taken with ICCDs at different timing over a series of shots. The upper and lower panels were taken with SG1 and SG2, respectively, and the panels in the same column were taken on the same shot. Figures 3(a) and (d) show the references of 3(b) and 3(e) before the shot, respectively. Figures 3(c) and (f) were taken on the same shot as in the right panel of Figure 2. The origin of the x-coordinate is determined from the nominal target position in each reference. While relatively smaller shadows are seen on the first (left) plane, broader shadows are seen on the second (right) plane in Figure 3. For instance, the solid lines representing the lateral size of plasmas in Figure 3(b) are 1 and 2 mm for the left and right plasmas, respectively. This is because we focused the laser on the first (left) plane with a focal spot size of 400 μm, and some portion of the laser penetrated the first target and defocused and ablated the second (right) plane. The geometrical beam size with an $F = 4$ system on the right plane is 750 μm. This ratio corresponds to the ratio of the beam sizes on the left and right planes. The plasma expansion from the first (left) plane is different from that of the second (right) plane; they are asymmetric. In a shadowgram an opaque region corresponds to a high-density region. It is also sensitive to the second derivative of the density in space; when there is a sharp density change such as a shock and contact surface, it shows a thin line along the structure. In Figure 3(e), which is 2.3 ns from the main laser, there are some thin lines in the transparent region in front of the opaque region near the right plane. From the SOP images in Figure 2 the counterstreaming plasmas start to interact from ~3 ns, and the low-density and large-velocity plasmas can start to interact even earlier (Kuramitsu et al. 2009). These lines are considered to be density structures resulting from the plasma interaction. Since the shadowgram is the image of transmitted light, when there are structures along

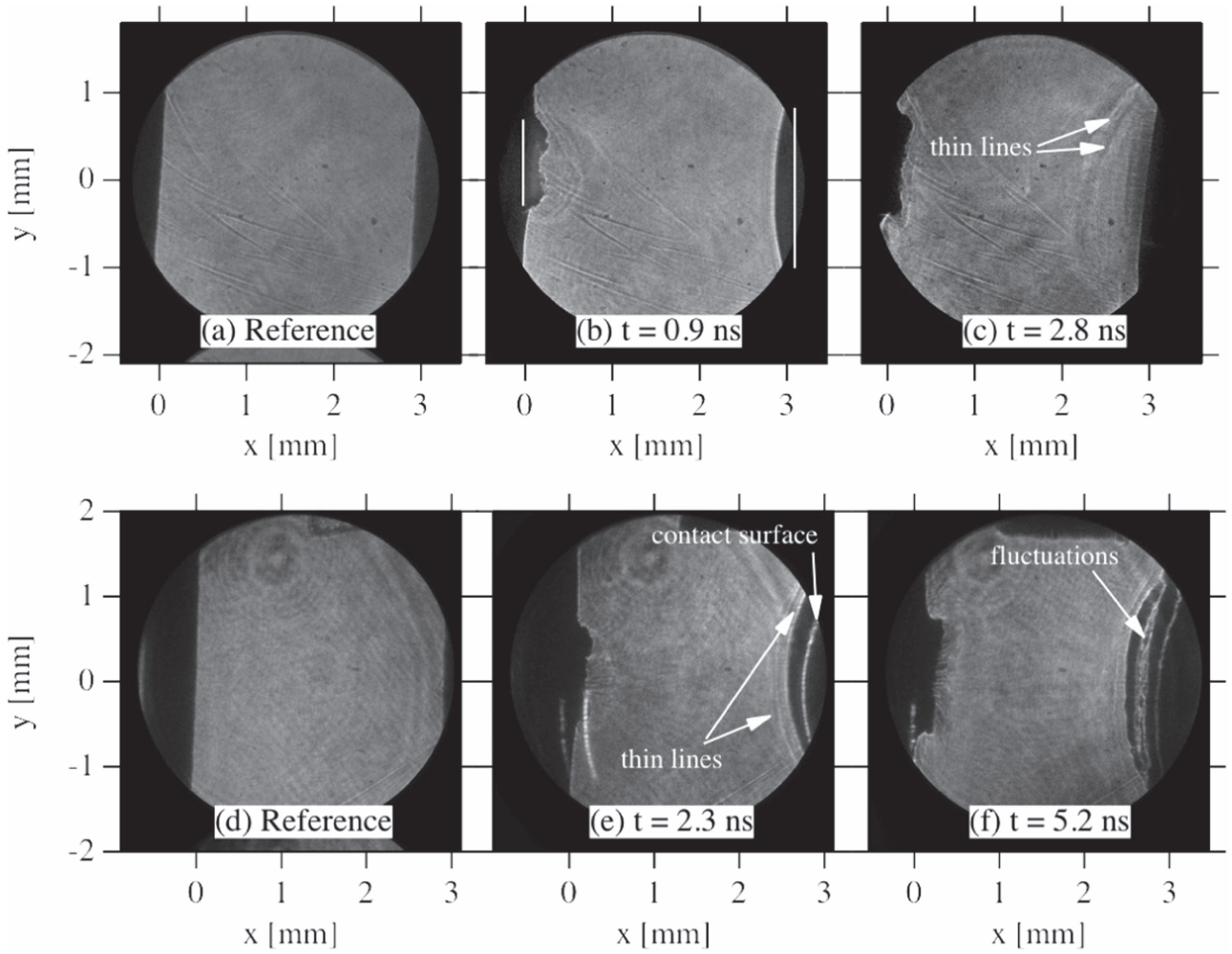

Figure 3. Series of shadowgrams taken on different shots. The upper and lower images are taken with SD1 and SD2, respectively.

the light pass, it shows several lines. Similar thin structures can be recognized at a later time in Figure 3(c). There is also a line of light in the opaque region in front of the second plane in Figure 3(e). The line of light is considered to be a contact surface between two plasmas. As evidence, some fluctuations appear from the line of light at a later time in Figure 3(f).

Figure 4 shows plots similar to those in Figure 3, but at later times. Figures 4(a) and (d) are taken on the same shot as the left panel of Figure 2. We can directly compare the SOP image and the shadowgrams. As we mentioned earlier the low-density and high-velocity plasmas can penetrate each other. In Figure 4(a) at $t = 4.9$ ns the opaque region of the rear plasma from the first (left) plane seems similar to the earlier images in Figure 3. However, in Figure 4(d) at $t = 7.3$ ns, when the transmitted part of the P2 plasma starts to interact with the plasma near the first plane, we can see a sharp density structure, which propagates in later times to the right as seen in Figures 4(b), (c), (e), and (f). The positions and timing are roughly consistent with the shock trajectory in the left panel of Figure 2.

The fluctuations within the thin transparent structures in the opaque regions seem to grow in time in Figures 4(a), (b), (d), and (e). In Figure 4(a) one can clearly see the wavelike structures in this region. In Figure 4(b) the amplitude of the wavelike structures becomes large and on the crest of the structures dark and circular features can be recognized. These grow in time and in Figure 3(e) we clearly see the circular features on the crests. These wavelike structures and circular features on the crests cannot be recognized further later times in Figures 4(c) and (f).

4. NUMERICAL SIMULATIONS

In order to understand how the plasmas are created, we need to simulate the laser–matter interactions, where the radiation plays an essential role. First we use the RHD code to simulate the laser–matter interactions. Using this result we re-map the physical quantities in a high-resolution HD code to investigate the hydrodynamic instability.

In the previous study (Kuramitsu et al. 2012) since there is a certain incident angle of the main laser, the fast ablation plasma from the second target was not observed. Thus, we turned off the laser after it transmitted the first plane, and then, only the radiation from the first plane irradiated the second plane. As a result, the plasma from the second plane was rather flat and had a low velocity and high density. Here we clearly see in the SOP images in Figure 2 the fast ablation plasma from the second plane. Now we simulate the interaction between the transmitted laser and the second plane with the RHD code.

4.1. RHD Simulation

We perform RHD simulations in cylindrical, symmetric two-spatial dimensions (Ohnishi et al. 2006). The laser conditions

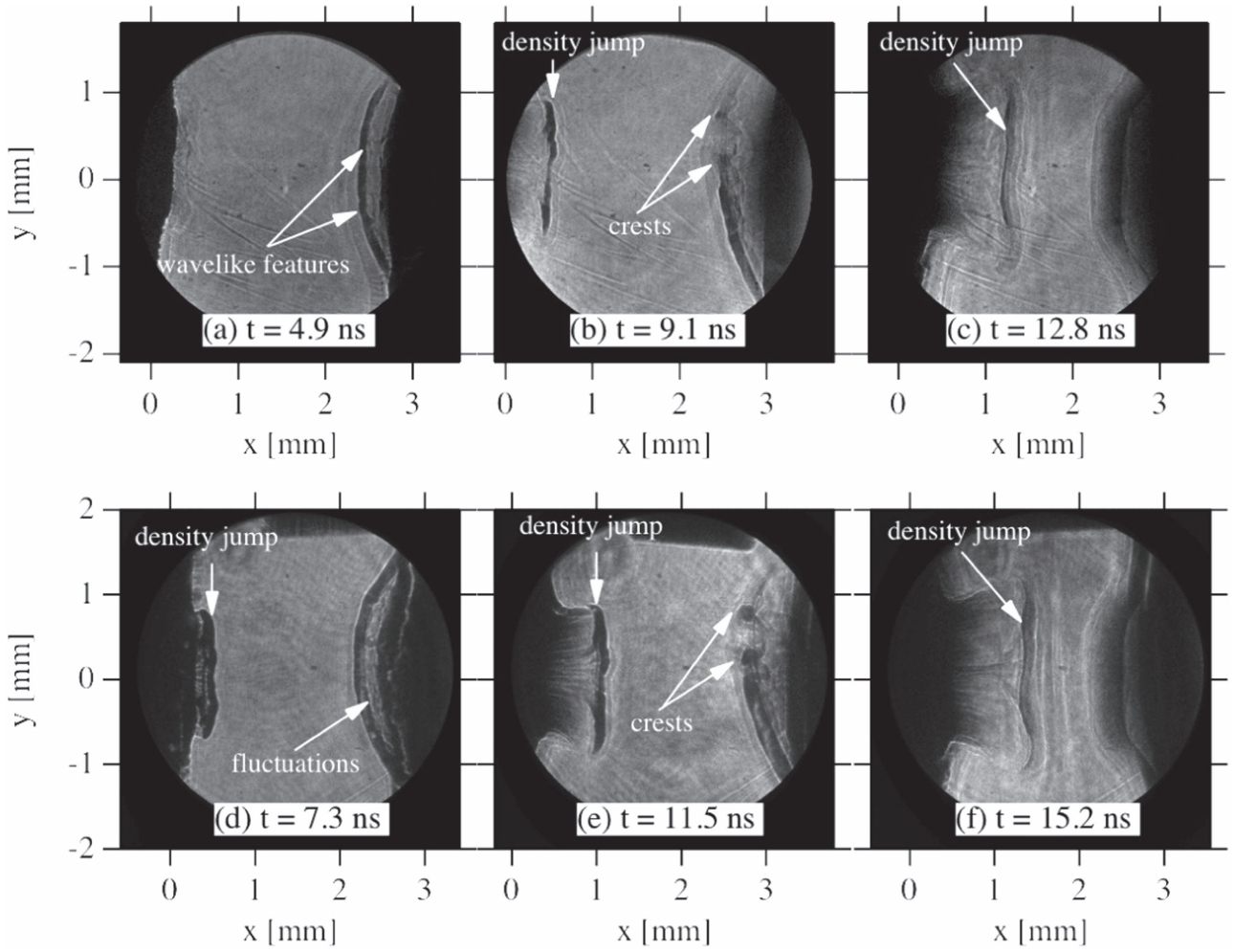

Figure 4. Same as Figure 3 except with later timings.

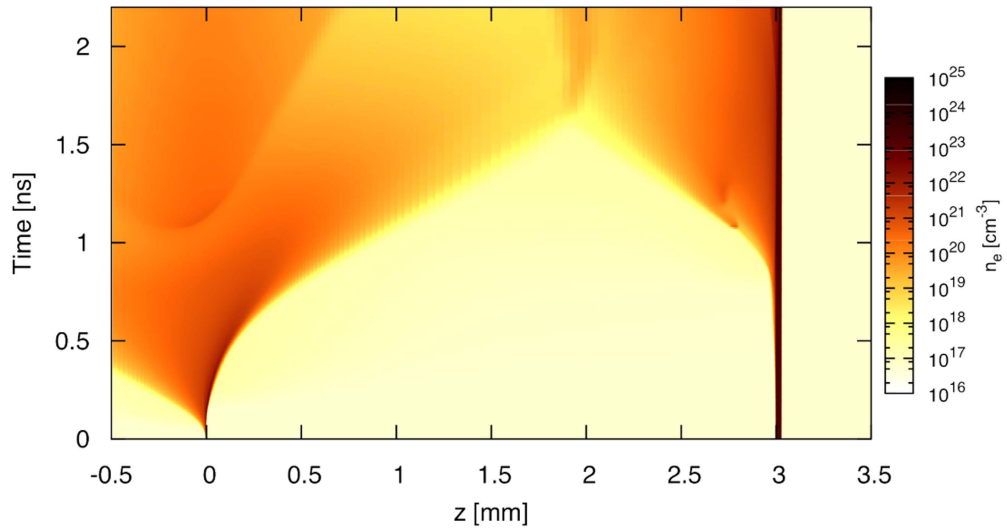

Figure 5. Time evolution of the plasma density on the axis in the RHD simulation.

are the same as in Kuramitsu et al. (2012), with an energy of 300 J, a focal spot of 400 μm, and a pulse duration of 1.5 ns. In order to roughly adjust the plasma expansion from the first plane, we reduced the laser intensity by increasing the pulse duration, keeping the laser energy constant. There is a limitation in the RHD simulation; due to our finite computer resources we assume straight propagations of rays. There is no defocusing of the laser in our RHD system. Therefore, the plasma from the second plane is faster and has a smaller region of ablation than those in the experiments, and the interaction

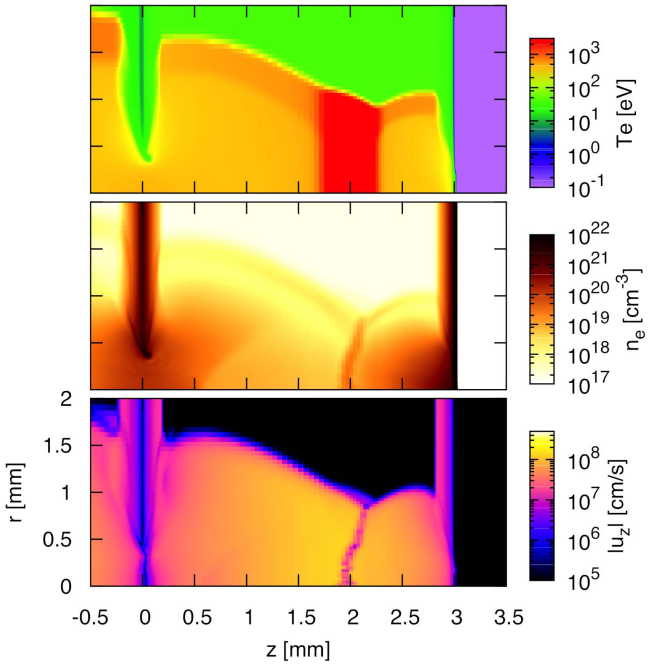

Figure 6. RHD simulation showing snapshots of (a) electron temperature, (b) electron density, and (c) absolute value of the z component of the velocity field at $t = 2$ ns. The laser comes from the left and the targets are placed at $x = 0$ and 3 mm.

point of counterstreaming plasmas can be different from that in the experiment. Nevertheless, the counterstreaming plasmas in the RHD simulation are still asymmetric and we can see the hydrodynamic instability due to the asymmetry of the plasmas.

Figure 5 shows the time evolution of the plasma density along the axis. The laser is coming from the left in the image. The origin of time corresponds to the timing when the edge of the laser starts to interact with the first plane. As seen in Figure 5 the laser irradiates the front side of the first plane and after a finite time (~0.2 ns) the rear side of the plasma is recognized. In the very beginning the ablation plasma expands much faster than the rear plasma. If there is a finite displacement between the plasma axis and the imaging slit of the SOP, one can expect a further delay on the rear emission, as seen in Figure 2. The transmitted light ablates the second plane and the ablation plasma starts to expand from $t \sim 0.8$ ns. This qualitatively explains the delay of the plasma emission from the second plane in Figure 2. There is a finite density range where the SOP is sensitive (Kuramitsu et al. 2009). This can also enhance the delays in the SOP image (Figure 2). The two plasmas start to interact at $t \sim 1.7$ ns in Figure 5. This is overestimated since the velocity of the ablation plasma from the second (right) target is overestimated. However, taking into account the time delay (~0.5 ns) between the experiment (Figure 2) and the simulation (Figure 5), and the fact that the SOP cannot observe low density plasmas, this is not too early.

Figure 6 shows snapshots of (a) the electron temperature, (b) the electron density, and (c) the absolute value of the z-component of the plasma velocity from the RHD simulations at $t = 2$ ns. As mentioned above, the laser rays propagate straight, and thus, the radial expansion and the velocity of the ablation plasma from the second target is under- and overestimated, respectively. However, the velocities, densities, and expansions of the two plasmas are different, therefore, we can qualitatively discuss the consequences of interactions of the asymmetric counterstreaming plasmas. The upstream (downstream) on the axis temperature, density, and velocity of the rear plasma from the first plane are a few hundreds of eV (a few keV), ~10^{18} cm^{-3} (~10^{19} cm^{-3}), and ~1000 km s^{-1} (~10–100 km s^{-1}) at this time. Regarding the plasma from the second plane, the temperature is lower, the density is higher, and the velocity is slower than those of the first plane. In the experiment, since the laser is focused on the first plane and defocused on the second plane, the ablation plasma from the second plane has an even lower temperature and velocity.

Figure 7 shows the time evolution of the ion (T_i) and electron temperatures (T_e) (a), (c), (e), and the effective charge state (Z) (b), (d), (f) at 1 ns (top), 1.5 ns (middle), and 2 ns (bottom). The laser is so intense that the ionization state quickly reaches its maximum, $Z = 13$, less than 0.1 ns (no shown), and stably expands as in Figure 7(b). As time passes, the Z value starts to slowly decrease as in Figure 7(d). When the two plasmas interact, forming shocks, the downstream temperature increases and Z becomes ~13. The upstream Z value reduces to ~11. At the end of the RHD simulation, the Z is flat in space and in order to resolve the hydrodynamic instability we remap these results into an HD simulation. When the ionization is greatly different in the upstream and downstream, for instance, $Z \sim 1$ becomes 2, as in Moser & Hsu (2015), the ionization and radiation effects are not negligible. However, in our experiment the difference is small, $13/11$. Moreover, $Z \sim 11$ is in a relatively stable state over a wide rage (tens of eV to hundreds of eV) in corona equilibrium or even in local thermal equilibrium (Chapter 5 of Salzmann 1998). We assume a constant Z and remap the RHD results into a high-resolution HD simulation.

4.2. Hydrodynamic Simulations

Additional numerical HD simulations have been done to follow the growth of nonlinear KHI. The result of the RHD simulation at $t = 2.0$ ns shown above is remapped onto much higher resolution grid points. This calculation allows us to see the fate of the perturbation generated by the interaction of the two shocks. Then, the HD calculation is done by using a code in which the modern shock capturing a Godunov-type scheme is employed (Mizuta et al. 2002). We assume ideal plasma with a constant specific heat ratio of $5/3$ and any radiative processes are ignored. The calculation does not include the incident laser since the laser has already been turned off at this point. The cylindrical coordinate ($r \times z$) with grid points ($N_r = 1700$, $N_z = 3000$, and $\Delta r = 2.35 \times 10^{-4}$ cm, $\Delta z = 2 \times 10^{-4}$cm) is used. The radial outer boundary is extended to 4 mm. The reflective boundary condition is employed at cylindrical axis and the zero gradient boundary condition is enforced at other boundaries.

Figure 8 shows snapshots of the mass density (upper) and the z component of the plasma velocity (lower) at different times $t = 3.0$, 5.0, 7.0, 9.0, 11.0, and 13.0 ns. In the color scale of the velocity field, the white color corresponds to $u_x = 0$. Due to the asymmetry of the plasma densities, velocities, and structures, there is shear along the contact surface (not shown). At this stage there are already some fluctuations along the contact surface due to the KH instability. Note that as we mentioned the time evolution of the plasma dynamics can be earlier than that of the experiment. In Figure 8(b) the fluctuations grow and form vortices. Since there are some structures in shock fronts in the RHD simulation in Figure 6, some vortices show an

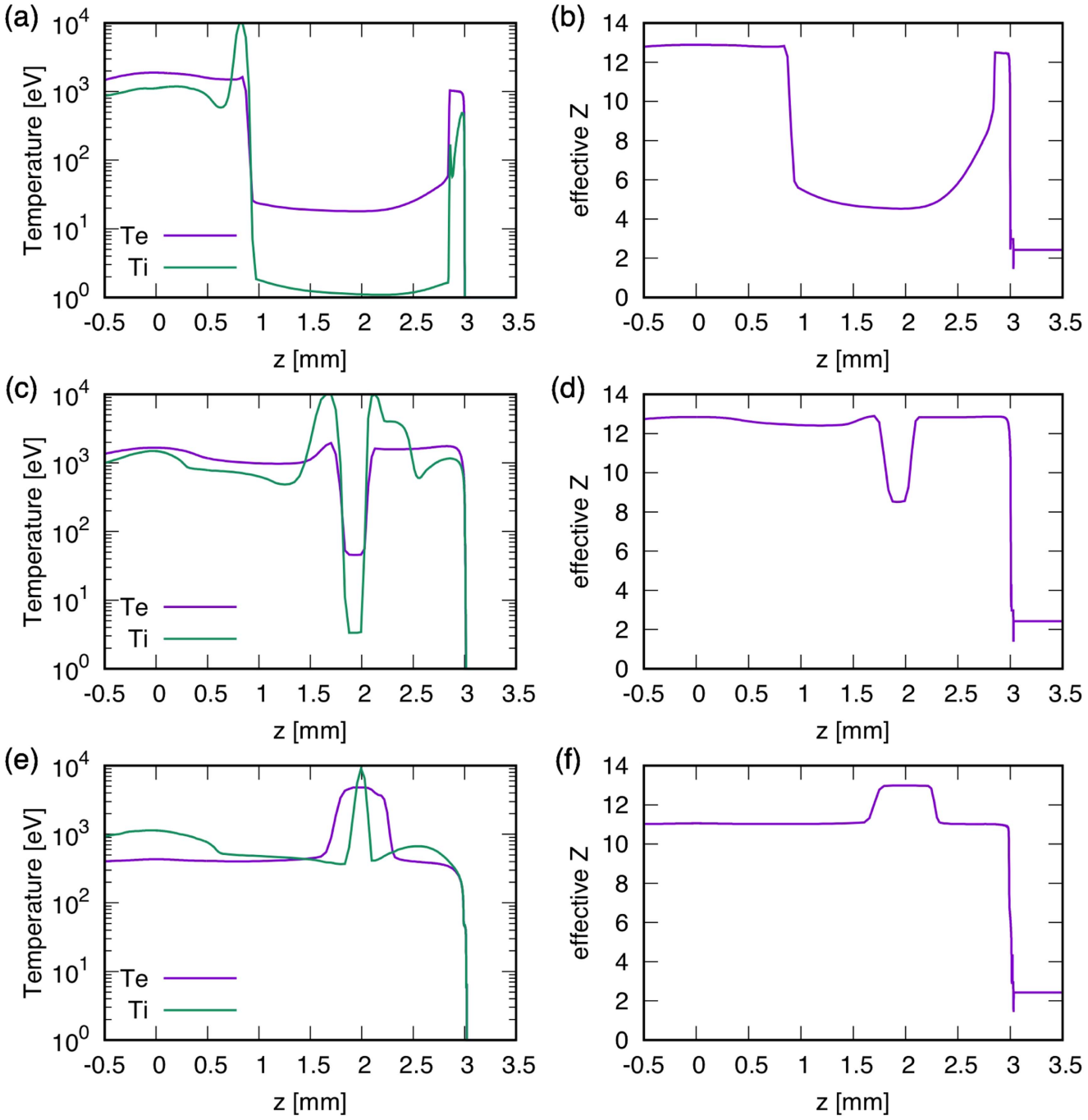

Figure 7. Time evolutions of on-axis plasma temperatures (left panels) and effective ionization (right panels) at (a) and (b) 1 ns, (c) and (d) 1.5 ns, and (e) and (f) 2 ns.

opposite vorticity. As time passes only one direction of the vorticity survives in each half-panel and clear vortices are developed in Figure 8(c). In Figure 8(d) further windings of the vortices clearly show circular features. These circular features smear later times in Figures 8(e) and (f).

Finally we show the radial component of the velocity field in Figure 9(a) at 3 ns and (b) 5 ns, which corresponds to Figures 8 (a) and (b), respectively. In the downstream regions there are strong shear flows of several hundreds of $\mathrm{km\,s^{-1}}$. Note that along the symmetry axis ($r = 0$) there is little velocity jump in the radial component where the shock is parallel to the r axis. The velocity component normal to the shock surface is shocked and slows down in the downstream. The total velocity fields are rather tangential and normal to the shock in the plasma from the first (left) and the second (right) planes, respectively. This results in the velocity shear that excites KHI.

5. DISCUSSION AND SUMMARY

In a previous experiment (Kuramitsu et al. 2012) we used proton radiography to observe the electric/magnetic field at the collisionless shock waves. We also showed the interferograms at two different timings to estimate the mean free paths which were larger than the structure sizes. In this experiment we focused on measuring the time evolution of the counter-streaming plasmas, shock formations, and resultant KH vortices by using SOP and by obtaining the shadowgrams

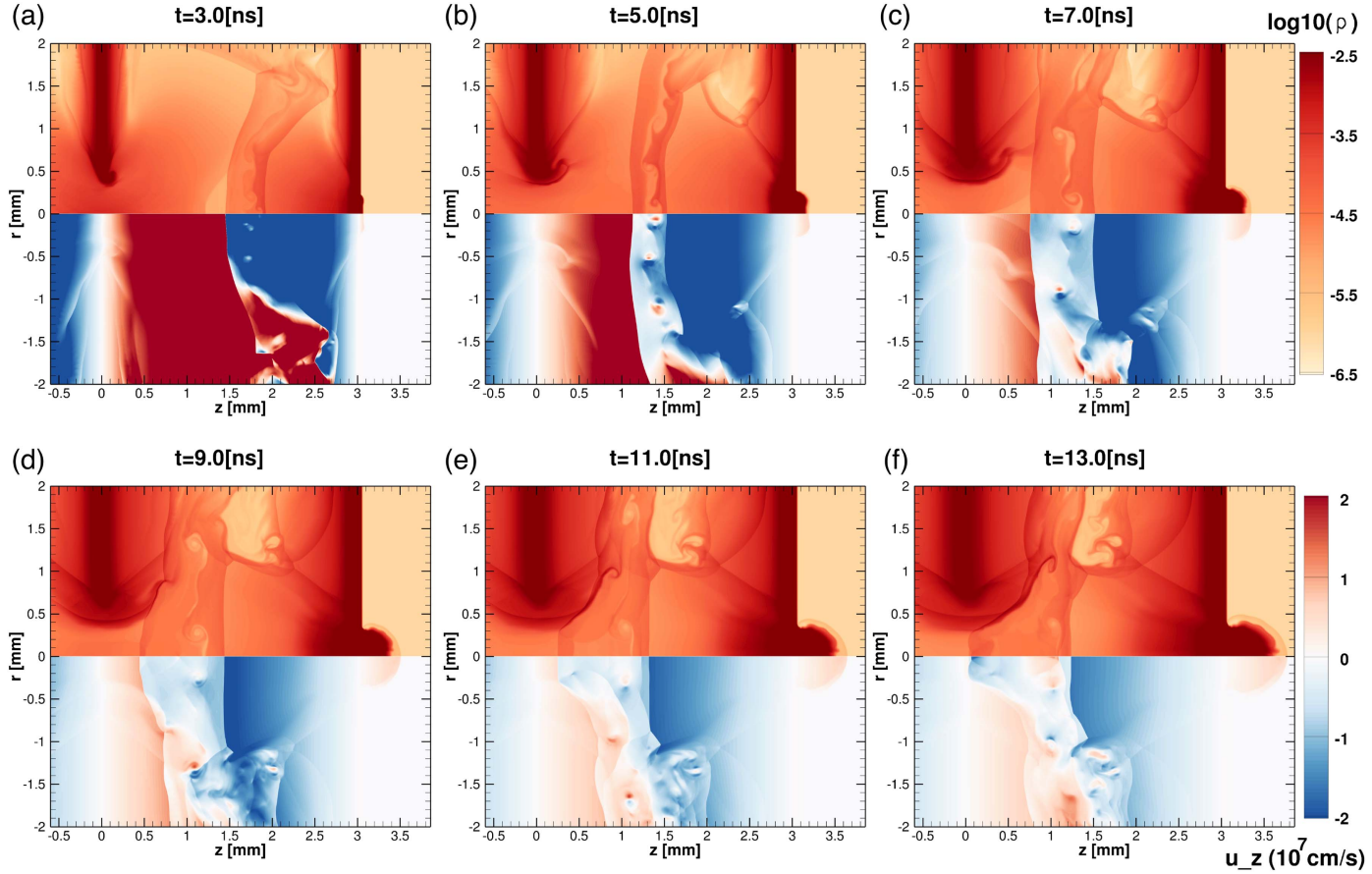

Figure 8. HD simulation results. The time evolution of the mass density in g cm^{-3} and the z component of the plasma velocity in cm s^{-1} are shown in the upper and lower panels, respectively: at (a) $t = 3$ ns, (b) $t = 5$ ns, (c) $t = 7$ ns, (d) $t = 9$ ns, (e) $t = 11$ ns, and (f) $t = 13$ ns.

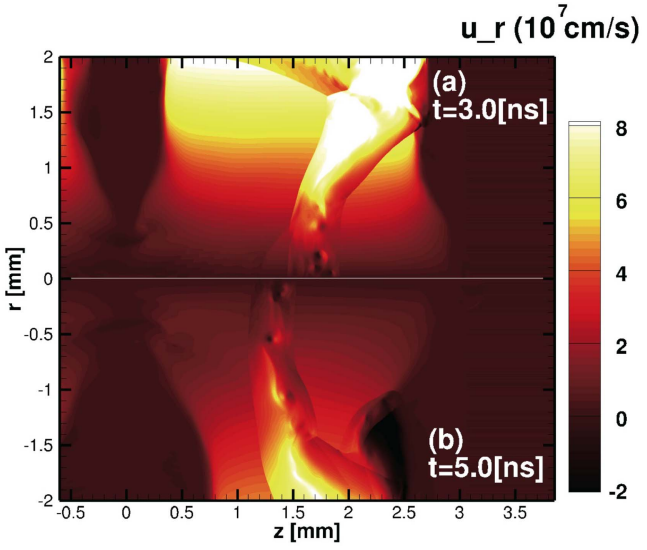

Figure 9. The radial components of velocities u_r are plotted at (a) 3 ns in the upper plane and (b) 5 ns in the lower plane, respectively. The velocity shear in the radial direction is several hundreds of km s^{-1}.

over shots. The shadowgraphy with wavelength shorter than the previous experiment clearly shows the transverse fluctuations and circular features evolving in time. From the relevant numerical simulations, these fluctuations and the circular features are considered to be excited by the KHI and the resultant vortices.

It is hard to determine the wavelength of the fluctuations observed at early times in shadowgrams in Figures 3(f) and 4 (d). At later times the wavelength is estimated from the crests on the wavelike features as 0.5–1 mm in Figures 4(b) and (e). These are consistent with the numerical results, where the distance vortex to vortex is also 0.5–1 mm. The plasma velocity observed in SOP images in Figure 2 shows the velocity component normal to the target. The minimum velocity to reach 2 mm in 10 ns, which roughly corresponds to shock position, has to be 200 km s^{-1}. The normal component of plasma velocity from the first plane is estimated from Figure 2 as 200–850 km s^{-1}. In the shadowgrams in Figures 3 and 4 the structures interested such as the contact surface, wavelike features, and crests are in $x \sim 2.5$ mm. This distance divided by the observed time provides similar velocity range. The transverse scale of the structures are about ± 1 mm. Thus, the transverse velocity is estimated by multiplying $1/2.5$ to the normal component as 80–340 km s^{-1}. Since the shock surface is mainly parallel to the target, the normal velocity component is shocked and slows down, however, the transverse component does not. In the same way, the plasma velocity from the second target is roughly estimated by multiplying $0.5/2.5$ to the plasma velocity from the first plane. The transverse velocity component from the second plane is about 16–68 km s^{-1}. The difference between the transverse components from both planes is the shear flow along the contact surface, which is 64–272 km s^{-1}. In the shadowgrams Figures 3 and 4 the thin lines and contact surface have curvatures, and therefore, the downstream velocities from the first and second targets can be

Table 1
Order Estimation of Mean Free Path of Plasma Particles

	P1 to P2	US to DS	US	DS
$\langle v_i \rangle$ (km s^{-1})	1600	850	v_{Ti}	v_{Ti}
T_i (keV)	0.5	10	0.5	10
$n_e = Zn_i$ (10^{18} cm^{-3})	0.1	1–10	0.1–1	1–10
Z	11	13	11	13
λ_{ii} (mm)	5.1×10^3	3.1–28	0.58–4.9 $\times 10^{-3}$	10–89 $\times 10^{-3}$
$\langle v_e \rangle$	$(\langle v_i \rangle^2 + v_{Te}^2)^{1/2}$	$(\langle v_i \rangle^2 + v_{Te}^2)^{1/2}$	v_{Te}	v_{Te}
T_e (keV)	0.5	5	0.5	5
λ_{ee} (mm)	4.2	3.6–33	0.44–4	3.6–33
Λ (10^5)	…	…	1.6–5.2	5.8–18

faster and slower than the estimations, respectively. The velocity shear along the contact can be larger than the above estimation. This is also consistent with the HD simulation, where the shear is about several hundreds of km s^{-1} as in Figure 9. The density difference across the contact surface cannot be directly measured from the shadowgrams or SOP images. However, assuming the emissions in SOP images in Figure 2 proportional to the square of the plasma density, the plasmas from the first and second planes have similar densities. Since the interaction point or contact surface is closer to the second plane, the density from the second plasma is considered to be higher than that of the first plane but of the same order. With the observed wavelength 0.5 $\sim$ 1 mm, the estimated shear $|v_1 - v_2|$ as 100–300 km s^{-1}, and the density difference $\rho_2 \sim \rho_1$–$5\rho_1$, the timescale for KHI to grow with $\gamma_{\rm KH}^{-1}$ is estimated as 1–3 ns, which is consistent with our observations, that is, the wavelike features appear $\sim$2 ns after the two plasmas start to interact.

We estimate the mean free path of particles by using four different average velocities as listed in Table 1. The four different cases are: (1) the counterstreaming relative velocity (P1 to P2) observed with SOP in Figure 2, (2) the relative velocity from upstream to downstream particles (US to DS), (3) the internal velocity in the upstream plasma (US), and (4) the internal velocity in the downstream plasma (DS). The first case corresponds to the very beginning of the plasma interaction when the fast plasmas encounter each other. The second case is relevant to whether the shock is collisionless, and we use the P1 velocity in Figure 2 as the upstream bulk velocity and assume that the downstream is at rest since the contact seems at rest in Figures 3 and 4. In these two cases, while the ion thermal velocities are negligible, the electron thermal velocities are taken into account. Indeed the balk velocity is negligible to estimate the electron–electron mean free path (λ_{ee}). For the internal average velocity we use the thermal velocities of ions and electrons. The ion and electron temperatures (T_i and T_e) and the effective ionization are adopted from the RHD simulation in Figures 7(e) and (f). The electron number density is considered to be similar to that in the last experiment (Kuramitsu et al. 2012), which is also consistent with the RHD result in Figure 5. The ion–ion mean free paths (λ_{ii}) of fast counterstreaming and also upstream to downstream plasma are essentially much larger than the shock width, which is characterized by the thin structures in the shadowgrams in Figure 3. Therefore, there must be an electric or magnetic field to form the collisionless shock (Kuramitsu et al. 2012). On the other hand, the internal mean free paths of ions are mush smaller than our system size. The hydrodynamic description of downstream plasmas is appropriate. Note that the plasma parameter $\Lambda \equiv 4\pi\lambda_D^3 n_e \propto \omega_{pe}/\nu_{ei}$, where ν_{ei} is the electron–ion collision frequency, is of the order of 10^{5-6}; the corrective effects are dominant over the random collisional processes.

The numerical simulations qualitatively explain the experimental results: the production of the asymmetric counterstreaming plasmas, shock formation, excitation of KHI, and resultant vortices. The time evolution of the plasma dynamics is well reproduced by numerical simulations. As we mentioned earlier, however, there are several limitations in numerical simulations due to our finite computer resources. First, due to the two-dimensionality the simulation systems are cylindrical symmetry. This makes the plasma evolutions in simulations "cleaner" than in the experiment. Moreover, the downstreams of the shocks become turbulent as KH instability grows. We cannot expect the system to stay symmetric in such turbulence. This is one of the reasons why the transverse fluctuations and the circular features, which are considered to be KH vortices, disappeared in later times (Figures 4(c) and (f)).

The second limitation is the straight propagations of the laser rays. In the experiment we focus the main beam with an $F = 4$ system on to the first target. The laser transmitted in the first plane is defocused in the second plane, which is 3 mm away from the first plane. A simple geometrical estimation gives a 750 um diameter of the laser at the second plane. One can see this, for example, in Figure 3(b); the opaque dense plasma region of the second plane is about twice as large as that of the first plane. The laser intensity is inversely proportional to the laser spot size, which is kept constant in the simulation. The intensity in simulations is four times more overestimated than that of the experiment. Since the temperature of the laser-produced plasma is proportional to the laser intensity and the plasma velocity is proportional to the thermal velocity of the plasma, the velocity from the second plane in the simulations is two times more overestimated than that of the experiment. Since the total mass ablated with laser is proportional to the laser energy, which is nominally identical both in simulation and experiment, the momentum density from the second plane in the simulations is further overestimated. Because of this, all the structures of the shocks and contact surface propagate to the left in the simulation (Figure 8), which seems faster than in the experiment. This is one of the reasons why the KH vortices smear in the simulation in Figures 8(e) and (f).

The third limitation, which is not mentioned above, is that the penetration of plasmas is not described with our current codes. As the experimental results show in Figure 2 some part of the plasmas with low density and high velocity can penetrate each other. This also excites the shock near the first target, which propagates from the left to the right. This does not directly affect the shock near the second plane on which we mainly focus in this paper. When we need to simulate a much longer time evolution of counterstreaming plasmas and shocks, we have to consider this mutual penetration. To this end we are planning to develop the RHD code for rarefied plasmas.

When two supersonic plasmas interact, two shock waves result. In general, these two plasmas and thus the shocks are different from each other in space/astrophysical and also laboratory plasmas. This creates shear flow along the contact surface of the two plasmas, resulting in KHI. Since the shock waves are ubiquitous in the universe, the KHI can universally

take places in the downstream of shocks along the contact surfaces. The KH vortices can mix two plasmas and thus play essential roles in plasma transport (Hasegawa et al. 2004). The KH vortices can also be a source of turbulence, which is also observed in various space/astrophysical phenomena. As seen in Figures 8(d)–(f) the large-scale vortices can affect the shock structure, which can modify the particle reflections at the shock front (Burgess 2006). The shock surface fluctuations due to KH vortices are more eminent in the previous experiment (Kuramitsu et al. 2012).

In the previous experiment (Kuramitsu et al. 2012) we interpret the proton image by assuming a turbulent electric field excited via the KHI. This can be a turbulent magnetic field. Recent PIC simulations in electron scale show magnetic field generation from the null field due to KHI (Alves et al. 2012). If the KHI driven magnetic field can survive in ion scale, it is interesting to investigate this as an origin of magnetic field in the universe (Kuramitsu et al. 2015).

The authors are grateful for the technical support of the staff at the LULI and M. Hoshino for valuable discussions. This work was supported by JSPS KAKENHI Grant Numbers 24740369, 21340172, and 15K17670; a grant for the Core-to-Core Program from JSPS; by the Asian Core Program for High Energy Density Science Using Intense Laser Photons commissioned by JSPS; and by the Ministry of Science and Technology, Taiwan, under Grant No. MOST-103-2112-M-008-001-MY2 and MOST 104-2911-I-008-504. The authors thank ISSI for support to attend the workshop "Physics of the Injection of Particle Acceleration at Astrophysical, Heliospheric, and Laboratory Collisionless Shocks."

REFERENCES

Alves, E. P., Grismayer, T., Martins, S. F., et al. 2012, ApJL, 746, L14
Berné, O., Marcelino, N., & Cernicharo, J. 2010, Natur, 466, 947
Burgess, D. 2006, ApJ, 653, 316
Doss, F. W., Fincke, J. R., Loomis, E. N., Welser-Sherrill, L., & Flippo, K. A. 2013a, PhPl, 20, 122704
Doss, F. W., Kline, J. L., Flippo, K. A., et al. 2015, PhPl, 22, 056303
Doss, F. W., Loomis, E. N., Welser-Sherrill, L., et al. 2013b, PhPl, 20, 012707
Drake, R. P. 1999, JGR, 104, 14505
Drake, R. P. 2006, in High-Energy-Density Physics: Fundamentals, Inertial Fusion, and Experimental Astrophysics, ed. L. Davison & Y. Horie (Berlin: Springer)
Elmegreen, B. G. 1998, in ASP Conf. Ser. 148, Origins, ed. C. E. Woodward, J. M. Shull, & H. A. Thronson, Jr., (San Francisco, CA: ASP), 150
Fox, W., Fiksel, G., Bhattacharjee, A., et al. 2013, PhRvL, 111, 225002
Harding, E. C., Hansen, J. F., Hurricane, O. A., et al. 2009, PhRvL, 103, 045005
Hasegawa, H., Fujimoto, M., Phan, T.-D., et al. 2004, Natur, 430, 755
Huntington, C. M., Fiuza, F., Ross, J. S., et al. 2015, NatPh, 11, 173
Hurricane, O. A., Hansen, J. F., Harding, E. C., et al. 2010, Ap&SS, 336, 139
Hurricane, O. A., Hansen, J. F., Robey, H. F., et al. 2009, PhPl, 16, 056305
Hurricane, O. A., Smalyuk, V. A., Raman, K., et al. 2012, PhRvL, 109, 155004
Kugland, N. L., Ryutov, D. D., Chang, P.-Y., et al. 2012, NatPh, 8, 809
Kuramitsu, Y., Chu, H.-H., Hau, L.-N., et al. 2015, HEDP, 17, 198
Kuramitsu, Y., Sakawa, Y., Dono, S., et al. 2012, PhRvL, 108, 195004
Kuramitsu, Y., Sakawa, Y., Morita, T., et al. 2011, PhRvL, 106, 175002
Kuramitsu, Y., Sakawa, Y., Morita, T., et al. 2013, HEDP, 9, 222
Kuramitsu, Y., Sakawa, Y., Waugh, J. N., et al. 2009, ApJL, 707, L137
Merritt, E. C., Doss, F. W., Loomis, E. N., Flippo, K. A., & Kline, J. L. 2015, PhPl, 22, 062306
Mizuta, A., Yamada, S., & Takabe, H. 2002, ApJ, 567, 635
Morita, T., Sakawa, Y., Kuramitsu, Y., et al. 2010, PhPl, 17, 122702
Morita, T., Sakawa, Y., Tomita, K., et al. 2013, PhPl, 20, 092115
Moser, A. L., & Hsu, S. C. 2015, PhPl, 22, 055707
Ohnishi, N., Nishikino, M., & Sasaki, A. 2006, JPhy4, 133, 1193
Park, H.-S., Huntington, C. M., Fiuza, F., et al. 2015, PhPl, 22, 056311
Remington, B. A., Arnett, D., Drake, R. P., & Takabe, H. 1999, Sci, 284, 1488
Remington, B. A., Drake, R. P., & Ryutov, D. D. 2006, RvMP, 78, 755
Ross, J. S., Glenzer, S. H., Amendt, P., et al. 2012, PhPl, 19, 056501
Salzmann, D. 1998, Atomic Physics in Hot Plasmas (Oxford: Oxford Univ. Press)
Takabe, H., Kato, T. N., Sakawa, Y., et al. 2008, PPCF, 50, 124057
Takabe, H., Nagatomo, H., Sunahara, A., et al. 1999, PPCF, 41, A75
Wang, P., Zhou, Y., MacLaren, S. A., et al. 2015, PhPl, 22, 112701
Yuan, D., Li, Y., Liu, X., et al. 2013, HEDP, 9, 239